Light Metals 2015
Edited by: Margaret Hyland
TMS (The Minerals, Metals & Materials Society), 2015

Light Metals 2015

ALUMINUM REDUCTION TECHNOLOGY

Modelling

SESSION CHAIR
Mark Cooksey
CSIRO
Clayton South, Australia

Light Metals 2015
Edited by: Margaret Hyland
TMS (The Minerals, Metals & Materials Society), 2015

3D COUPLED MHD AND THERMO-ELECTRICAL MODELLING APPLIED TO AP TECHNOLOGY POTS

S. Langlois[1], J. Rappaz[2], O. Martin[1], Y. Caratini[1], M. Flueck[2], A. Masserey[3], G. Steiner[3]

1- Rio Tinto Alcan, Laboratoire de Recherche des Fabrications, BP 114, 73303 Saint Jean de Maurienne, France
2 -Ecole Polytechnique Fédérale de Lausanne, Section Mathématiques, Station 8, FSB-EPFL, 1015 Lausanne, Switzerland
3-Ycoor Systems SA, Technopôle 10, 3960 Sierre, Switzerland

Keywords: Aluminium Reduction, MHD, 3D thermal-electric, thermal balance, AP4X

Abstract

A suite of efficient modelling tools is critical to continuously improve the performance and robustness of aluminium electrolysis cells. Rio Tinto Alcan has developed a suite of chained models to provide a good electrical balance in busbar configuration, satisfactory MHD stability in the cells, and thermal balance ensuring the ledge protection of the lining. This paper presents a high level model which calculates all magnetic, electrical, thermal fields as well as liquid velocities and ledge formation, all in 3D. First developed in 2005 by EPFL, follow-up work has improved mesh quality and performance, to give more reliable and accurate results. This MHD-TE model is now in an industrial form, using a qualified material database. Its capability to provide the measured values has been demonstrated on AP Technology pots. Cell designs can be better optimized to balance local effects observed on upstream/downstream sides, corners or end walls.

Introduction

A suite of efficient modelling tools is critical to continuously improve the performance and robustness of aluminium electrolysis cells. Rio Tinto Alcan (RTA) has developed a suite of chained models to provide good electrical balance in busbar configuration, satisfactory MHD stability in the cells, and thermal balance ensuring the ledge protection of the lining.
To predict some local thermal effects, as observed on cell corners or on downstream/upstream sides where relevant differences can be measured on specific cell configurations, a thermo-electrical (TE) model assuming cell symmetry, as a slice or quarter model [1-4], presents limited capabilities. These models, of great interest for quick lining design purposes, have to be associated with upper level models which consider the magneto-hydrodynamic (MHD) impacts linked to the busbar configuration, the cell position in the potlines, and the magnetization of the pot shell. Other features such as alumina dissolution [5-6], magnetic cell stability [7] and bubble flow [8-10], can be coupled to get an efficient modelling package. All these topics are developed in the partnership between RTA, the Mathematical Department of EPFL and Ycoor around the Alucell software. Thanks to J. Rappaz and O. Martin who are in charge of this process.
Obviously, other CFD modelling tools are required for hall and pot ventilation or gas extraction issues, as well as thermo-mechanical models for shell deformation, superstructure resistance, anode cracking and casting. All these models are shared between RTA research centers, ARDC at Arvida and LRF in France, and many contributors are involved, such as UQAC in Quebec.

This paper presents a high level RTA model which calculates all magnetic, electrical and thermal fields, as well as liquid velocities and ledge formation in 3D. To highlight local thermal effects, this MHD-TE model considers the MHD flows as a priority and doesn't focus on the bubble-driven forces [8-10], or on the thermal effects of alumina dissolution [5-6]. Some relevant quality criteria are highlighted in order to get accurate results, converged and stable solutions and fast time calculations. The first required quality is the ability to process industrial cell cases. As mentioned by Zarouni and al [11], in house software requires significant development effort as commercial packages have to be adapted for specific needs. Therefore, the decision was taken to promote the 'easy way to use' by interfacing the commercial Ansys@ package to Alucell MHD-TE model. By using APDL in the Ansys pre-processing phase, the pot modelled description becomes generic, independent of the pot technology, and is just defined by an extension of the usual RTA slice TE model (MTE). Coherence between the slice and the full MHD-TE models is thus kept in the design process. The use of a similar, in house, material properties database, which considers thermal dependency and anisotropy of the physical properties, also reinforces this coherence. The mesh and material attribution of the pot design is then exported from Ansys to Alucell. For post-processing and calculations analysis, Ycoor has developed specific tools in Alucell, but also some bridges with commercial visualization tools, such as Ensight@. The figure below summarizes the pot design modelling process used for TE topics. This combines in house and commercial tools, in order to define the electrical busbar balance [12], the magnetic stability [7] and the thermo-electrical behavior of the pot.

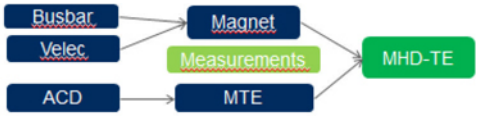

Figure 1: Modeling tools for MHD-TE design

MHD-TE Model

The equations governing the magneto-hydrodynamic (MHD) and thermo-electrical (TE) fields were solved by Safa in 2005 [13] by using a pseudo transient method to get steady state results.
The gravity ($\rho\vec{g}$) and Lorentz force ($\vec{j}\times\vec{B}$) are the driven forces involved in the MHD. Velocity and pressure fields fulfill the incompressible **Navier-Stokes equations**:

$$\begin{cases}\rho\frac{\partial\vec{u}}{\partial t}+\mathrm{div}\left(\tau(\vec{u},p)\right)+\rho(\vec{u}.\vec{\nabla})\vec{u}+K_\varepsilon\vec{u}=\vec{j}\times\vec{B}+\rho\vec{g}\\ \mathrm{div}(\vec{u})=0\end{cases} \quad (1)$$

With $\tau(\vec{u},p)$ the stress tensor $\tau(\vec{u},p)=2\mu\varepsilon(\vec{u})-p\mathbb{I}$ (2)

And the deformation velocity tensor:

$$\varepsilon(\vec{u})=\frac{1}{2}(\vec{\nabla}\vec{u}+(\vec{\nabla}\vec{u})^T) \quad (3)$$

The Carman-Kozeny coefficient, K_s, is introduced as a Darcy term to limit the fluid velocity when solidification occurs (ledge formation):

$$K_\varepsilon = \frac{C\mu(1-fl)^2}{(fl+\varepsilon)^3} \quad (4)$$

μ is the fluid viscosity, C and ε are constant, f_l the liquid fraction:

$$fl(T) = \begin{cases} 1 & if\ T \geq Tl \\ 0 & if\ T \leq Ts \\ \epsilon]0,1[& if\ Ts < T < Tl \end{cases} \quad (5)$$

Tl, Ts are respectively the liquidus and solidus temperatures.

The magnetic induction B field is the sum of an external contribution due to the neighbor cells, busbars and compensation current loops, and of an internal part coming from the current flow through the main simulation cell.
The **magnetic induction B** in the pot is calculated with a Biot-Savart formula:

$$\vec{B}(t,\vec{x}) = \frac{\mu_0}{4\pi}\int(\vec{J}(t,\vec{y}) \times \frac{\vec{x}-\vec{y}}{\|\vec{x}-\vec{y}\|^3})\,d\vec{y} \quad (6)$$

In 2009, G. Steiner [14] developed a method to include the variation of the magnetic induction in the model. It is based on the decomposition of the magnetic induction in a static term associated with the initial set-up of the pot and a fluctuation term representing the variations of B. A Schwarz algorithm, involving the mesh of two balls around the cell, is applied to solve the exterior problem.

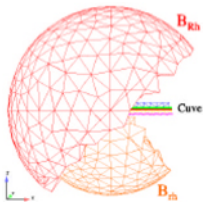

The resolution of the thermal problem follows a Chernoff schema [13] which implicitly solves the transition phase in the fluids by a relaxation method:

$$\frac{\partial H}{\partial t} + div(\lambda(T)\vec{\nabla}T) + \rho C_p\vec{u}.\vec{\nabla}T = \frac{\|\vec{J}\|^2}{\sigma(T)} \quad (7)$$

$$H(T) = \rho C_p T + Lfl(T) \quad (8)$$

To converge to steady state condition, a constant Cp value is attributed to all materials, so the solving method is pseudo-transient. The thermal conductivity in the fluids is weighted by the liquid fraction.
Some particular attention should be given to the discretization of the advection term. The energy conservation [15-16] must be developed for incompressible fluids at steady state: $div(\vec{u}.T) = 0$.
In addition, to prevent numerical oscillations of the diffusive-convective thermal schema, SUPG (Streamline Upwind Petrov Galerkin) methods are introduced [13, 15] to stabilize the solution and to limit the numerical diffusion when the Peclet number is greater than one, during the transition phase.
The applied thermal boundary conditions are differentiated on the upstream/downstream sides, the head sides and the corners. At different positions, x, around the pot, the involved heat transfer coefficients are temperature dependent to account for natural convection, radiation or other impacts such as forced cooling network (FCN) or gas extraction:

$$h(x,T) = a(x,T) + b(x,T).T \quad (9)$$

The values of the coefficients a, b, were determined by experiments.

Turbulence

As important velocity gradients occur in the fluids, turbulence effects can't be neglected. An extended Prandtl mixed length law, called Smagorinsky-Lilly model [17], is used to account for turbulence effects.

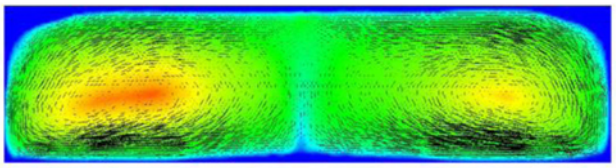

Figure 2: Example of velocity fields at bottom of metal

The anisotropic viscosity tensor μ, primarily defined with experimental values [18], now differentiates laminar and local turbulence impacts [14]:

$$\mu(x) = \mu_L + \mu_T = \mu_L + \varrho\alpha_t l^2\sqrt{2\epsilon(\vec{u}):\epsilon(\vec{u})} \quad (9)$$

with l a characteristic length depending on cell dimensions and α_t a coefficient preconized around 0.002.

By analogy, a turbulent thermal diffusivity is also added by assuming a turbulent Prandtl number around 0.6 for the metal:

$$\lambda(x) = \lambda_L + \lambda_T = \lambda_L + \frac{Cl^2}{Pr_T}\sqrt{2\epsilon(\vec{u}):\epsilon(\vec{u})} \quad (10)$$

A viscous heat dissipation term has also been added in the thermal equation, but a very limited impact has been shown. Note that other turbulent laws, such as Von Karman law, are currently tested in the alumina dissolution model [19] of Alucell.

Mesh Quality

Time step limitations are involved when solving Navier-Stokes and thermal equations. In relation to velocity fields, the mesh of the liquids was improved to get a pseudo CFL condition, which was nearly constant all around the mesh. The fluid mesh size was thus reduced near the side lining, where the flow velocities are maximum, and multiple layers were applied in both metal and bath phases.

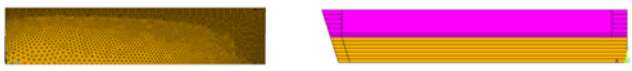

Figure 3: Liquid mesh on side and top ¼ views

Depending on the anisotropy of the conductivities of the lining materials, four size classes were defined in order to get a relatively similar diffusive time step, $\Delta t = \alpha/\Delta x^2$, when looking at the **characteristic dimensions** x of the materials.

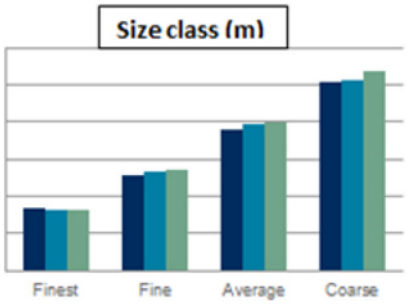

Figure 4: 4 class sizes of lining materials for AP designs

Consequently, by increasing the mesh quality, the CPU time limitations have been reduced by a factor of 3; the time step was increased from 1500 s to 5000 s, while increasing accuracy of the results and the stability of the solution. The same quality of results was also achieved when modelling different pot technologies or pot lining dimensions.

Front remesh

In order to simultaneously consider the deformation of bath metal interface and ledge formation, a front tracking method has been developed by Flotron [15]. For each time step, the algorithm detects the solidification front of the ledge and applies a local mesh refinement around the interface. This method is applied either for the solidification front or for the bath-metal interface when interface deformation is considered. The front, bath metal interface or solidification boundary, is determined by a level set method:

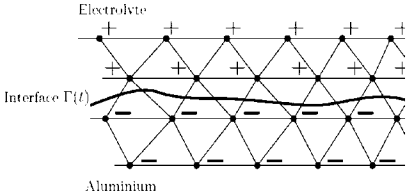

Figure 5 : Sign of the level relative to the position of the interface

It has been shown that the metal-bath deformation has no significant impact on the ledge formation in steady state. Therefore, a flat metal-bath interface can be considered when studying only the thermal effects and the ledge formation. However, when ledge formation is significant, this locally impacts the metal-bath interface deformation. As shown below, the interface deformation is significantly reduced on the boundaries:

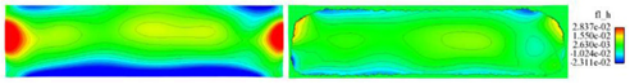

Figure 6: Metal-bath interface deformation (m) without (left) or with (right) ledge formation

Convergence and stability

Calculations have been automated when reaching the electrical and thermal balance in steady state. Electrical tuning coefficients, with values close to one, adjust the resistivity of the bath and anode/cathode cast iron in order to get the right pot controller voltage. BEMF voltage is calculated following formulae given in [20]. Bubble overvoltage takes into account the anode slot configuration by using a formula developed by GRIPS at UQAC[8-10]. Thermal balance is tuned by boundary conditions while taking into account:

- effects of the FCN and the pot ventilation,
- contact resistances if local insulation or gas layers are involved,
- material properties e.g. to adjust the covering powder granulometry.

Some 'degraded' properties can be applied when studying old pots. The thermal solution must verify the superheat but also the bath temperature distribution. For example, a 15°C variation was measured on bath temperature of an AP3X pot when stopping alumina feed:

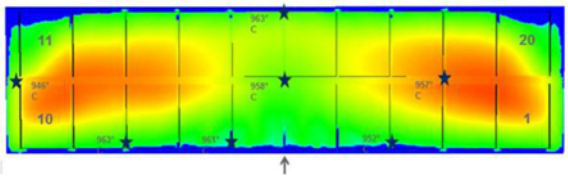

Figure 7: Temperature distribution in bath: AP3X

The figure 8 shows the exponential shape of the thermal evolution and the stability of the solution when thermal convergence is obtained: the total heat flux dissipated on the edges is then equal to the internal energy:

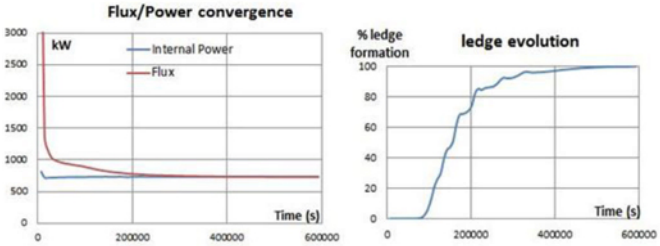

Figure 8: Convergence of flux, power and ledge formation

The solution is stable even when continuing the calculations, whether some operating conditions are changed or not.

Results

As CPU time has been decreased by a factor of 12 between 2009 and 2013, while increasing the quality of the results, the MHD-TE model is now available as a semi-industrial tool. It has been deployed on most AP technologies currently in operation in RTA plants: AP3X, AP4X, AP5X and APXe. The following illustrations show the comparison of the model results with measurements. Particular situations have been chosen to highlight local thermal effects due to MHD.

Magnetic field

Let us illustrate the magnetic modelling process on the figure 9, with an example from an RTA plant: first, define the halls of the plant, secondly, focus on the boosted section, and finally, choose the pot to study and calculate the magnetic fields.

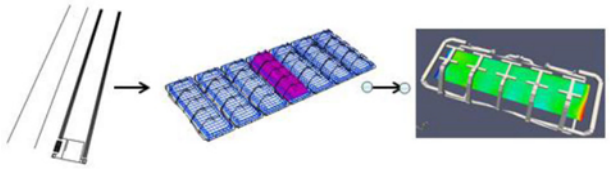

Figure 9: Process of magnetic modeling on AP40LE pot in boosted section

The calculated Bz induction fields referring to AP3X-AP4X pots operating in Rio Tinto Alcan plants are well correlated to measurements (Figure 10).

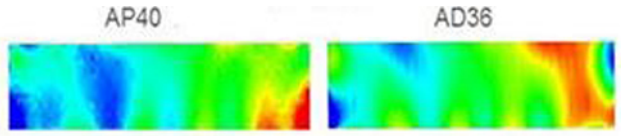

Figure 10: Bz induction modeled on AP3X pots

Fluid velocity field

As measured in the metal phase on an AP4X cell, the velocity field is maximum on the upstream corners and limited on the downstream ones. The maximum velocity modules are 16.3 cm/s with measurements, 16 cm/s from the model (Figure 11).

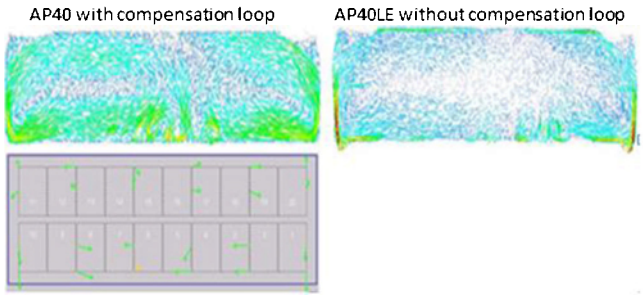

Figure 11: Velocity field modeled/measured in metal phase on AP4X pots

When comparing the modelled velocity fields of AP4X cells in two Rio Tinto Alcan plants, we can observe that velocity fields are maximum on the upstream corners in both cases. However, the velocity field is less marked on the downstream sidewall when a compensation loop is applied. This confirms the significant impact of the magnetic configuration of the pot on the metal velocity field: in this example, the position of the boosted section in the line and the existence of the compensation loop explain these differences.

Thermal field

When studying the shell temperatures of both AP40 and AP40LE cells, we can see, on the figure 12, that the upstream corners and heads are warmer, while downstream corners are colder. It is coherent with the previously shown vortex. The difference of temperature between downstream and upstream long sidewalls is more significant on the AP40LE pot. No FCN, forced cooling network, is applied on this Low Energy design. The calculated higher metal velocities near the downstream sidewall promote a warmer downstream shell.

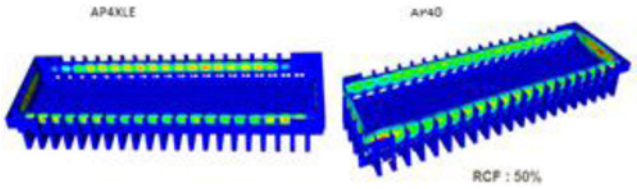

Figure 12: Shell thermal field on AP40LE and AP40 pots

These results are reliable for measurements, made on AP40LE pots, showing a warmer sidewall at the middle of the downstream side: a 40°C difference is found when comparing the shell temperatures around anode 14-15 (downstream) and anode 4-5 (upstream).

A good agreement between model results and measurements can also be shown on APXe cells operating in Hall Heroult at LRF, when studying the shell temperature profiles given at different anode positions (Figure 13).

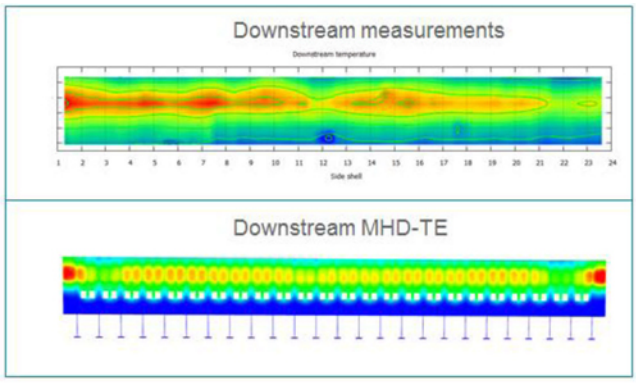

Figure 13: Temperature shell profile on APXe pot

We can see non-uniform hall ventilation during measurements: the right side of the downstream shell is slightly colder.

Ledge formation

The comparison of the modeled ledge formation with measurements is illustrated on Figure 14, on an AP40LE pot operating in relatively warm conditions.

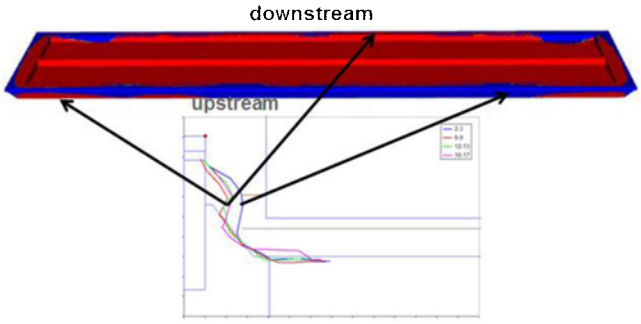

Figure 14: Ledge profile modeled on AP40LE pot

In accordance with previous views of velocity and shell temperature fields, we can observe more ledge protection, in blue color, on downstream corners and long upstream side, than on the middle of the downstream side and on upstream corners. The red color represents the metal/bath not solidified.

Therefore, specific attention to these potential ledge protection risks shown in the metal phase must be performed when improving the pot design.
Obviously, this modeled ledge formation, linked to MHD effects, can significantly change when modifying the operating parameters such as ACD, pot amperage, metal and cover heights, FCN conditions, or lining designs.
An optimized design is shown in Figure 15 which presents an AP40LE pot, operating in standard conditions in the boosted section.

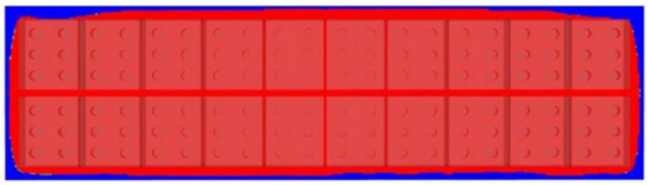

Figure 15: Ledge profile modeled on AP40LE pot

The ledge protection, represented in blue color, is well distributed all along the pot.

Conclusion

A summary of the partnership between EPF Lausanne, RTA modeling team and Ycoor is illustrated from the MHD-TE point of view. From 2009 to 2013, the quality criteria have been improved to achieve consistent, stable, non-diffusive numerical solutions, while also significantly optimizing the CPU performance and the ability to carry out industrial studies. As a result, the CPU time has been reduced from 20 days to 1.5 day. The MHD-TE model is now ready for industrial applications and deployment on most AP technologies has been performed. The other main developments in progress in Alucell package concern the improvement in turbulence laws near the walls, the introduction of bubble-driven forces and the alumina dissolution issues.
The MHD-TE model clearly shows the influence of the magnetic configuration and MHD on the thermal behavior of the pots. It has been well validated on operating pots, such as AP4X, AP5X, and APXe technologies. Some local improvements on the lining design, pot ventilation or cooling systems, can be clearly addressed by this model to better locally balance the thermal pot behavior when needed. This particularly concerns Low Energy designs which can involve thermal insulated barriers. In this way, the MHD-TE model is a 'good friend' of the slice TE model, usually used for RTA quick cell studies. It can provide added information to apply best criteria when studying the operating window of the cell.
Developing in house full 3D software requires substantial effort. The challenge also consists in generating reliable material properties databases, complete sets of local measurements, pot autopsies analyses, in order to feed the model data and improve the cell designs.

References

[1] Arkhipov GV, Pingin VV, Tretyakov YA, Polyakov PV, Simulation of Cell thermoelectric field with consideration of electrochemical processes, Light Metals, 2007, pp.327-331

[2] Knizhnik AV, Kuzakov AA, Zelberg BI, Veselkov VV, Application of mathematical methods to optimize Aluminium production in pre-baked anode cells, Light Metals, 2008, pp.437-442

[3] Cui X, Zhang H, Zou Z, Li J, Lai Y, Xu Y, Zhang H, Lv X, 3D Freeze Shape Study of the Aluminum Electrolysis Cells Using Finite Element Method, Light Metals, 2010, pp. 447-452

[4] Cui X, Zhou Y, Yang J, An improved finite element model for thermal balance analysis of Aluminum electrolysis cells, Light Metals, 2014, pp. 661-666

[5] Zhang H, Yang S, Zhang H, Li J, Xu Y, Numerical simulation of alumina-mixing process with a multicomponent flow model coupled with electromagnetic forces in aluminium reduction cells, Light Metals, 2014, pp. 1210-1217

[6] Hofer T, Numerical Simulation and Optimization of the Alumina Distribution in an Aluminium Electrolysis Pot, Thèse EPFL, n° 5023, 2011

[7] Renaudier S, Bardet B, Steiner G, Pedcenko A, Rappaz J, Molokov S, Masserey A, Unsteady MHD modeling applied to cell stability, Light Metals, 2013, pp. 579-585

[8] Yang S, Li J, Xu Y, Zhang H, Xiaojun LV, JIA M, A modelling of heat losses in Aluminium reduction cell with slotted anodes, Light Metals, 2014, pp. 667-672

[9] Poncsák S, Kiss L, Toulouse D, Perron A, Perron S, Size distribution of the bubbles in the Hall Heroult cells, Light Metals, 2006, pp. 457-463

[10] Kiss L, Poncsák S, Antille J, Simulation of the bubble layer in Aluminium Electrolysis cells, Light Metals, 2005, pp. 559-565

[11] Zarouni A, Mishra L, Bastaki M, Al Jasmi A, Arkhipov A, Potocnik V, Mathematical model validation of Aluminium electrolysis cell at Dubal, Light Metals, 2013, pp. 597-602

[12] Guerard S, Ouillon D, Pot-to-pot busbars thermo electric model, MS&T 2013, vol 2, pp. 1077-1085

[13] Safa Y, Simulation numérique des phénomènes thermiques et magnéto-hydrodynamiques dans une celle de Hall-Héroult, EPF Lausanne, Thèse n° 3185, 2005

[14] Steiner G, Simulation numérique de phénomènes MHD – Application à l'électrolyse de l'aluminium, EPF Lausanne, Thèse n° 4409, 2009

[15] Flotron S, Simulations numériques de phénomènes MHD thermique avec interface libre dans l'électrolyse de l'aluminium, EPF Lausanne, Thèse n° 5738, 2013

[16] Flotron S, Rappaz J, Conservation Schemes for convection-diffusion equations with Robin boundary conditions, ESAIM : Mathematical Modelling and Numerical Analysis / Volume 47 / Issue 06 / November 2013, pp 1765-1781

[17] Smagorinsky J, General Circulation Experiments with the Primitive Equations. I. The Basic Experiment, Month. Wea. Rev., 1963, 91, pp. 99-164

[18] Descloux J, Fluck M, and Romerio MV, A modelling of the stability of aluminium electrolysis cells - In Nonlinear partial differential equations and their applications., College de France Seminar, Vol. XIII (Paris, 1994/1996), vol. 391 of Pitman Res. Notes Math. Ser., p. 117-133. Longman, Harlow, 1998.

[19] Rochat J, Thesis in progress, EPF Lausanne

[20] Thonstad J, Fellner P, Haarberg GM, Hives J, Kvande H, Sterten A, Aluminium Electrolysis Fundamentals of the Hall-Heroult Process, Aluminium-Verlag 3d Edition, 2001